RSC Advances

PAPER

View Article Online
View Journal | View Issue

Cite this: *RSC Adv.*, 2022, **12**, 32142

Synthesis of Al/starch co-doped in CaO nanoparticles for enhanced catalytic and antimicrobial activities: experimental and DFT approaches

Muhammad Ikram, *[a] Ali Haider, [b] Syeda Tayaba Bibi,[c] Anwar Ul-Hamid, [d] Junaid Haider,[e] Iram Shahzadi,[f] Walid Nabgan, *[g] Sawaira Moeen,[a] Salamat Ali,[c] Souraya Goumri-Said [h] and Mohammed Benali Kanoun [i]

In this work, aluminum/starch (St)-doped CaO nanoparticles (NPs) were synthesized by a co-precipitation method to degrade harmful dyes in various pH media. Systematic characterization was performed to investigate the influence of Al/St dopants on the composition, crystal structure, functional groups present, optical characteristics, and morphology of CaO NPs. Further hybrid density functional analyses corroborated that the band gap energy was reduced as the Al concentration in starch-doped CaO is increased. Optical absorption spectra of the synthesized materials revealed a redshift upon doping, which indicated depletion in the band gap energy of Al/St-doped CaO. PL spectroscopy showed that the intensity of CaO was reduced by the incorporation of Al and St assigned to minimum electron–hole pair recombination. Interlayer spacing and morphological features were determined by HR-TEM. HRTEM revealed that the control sample has cubic NPs and the incorporation of St showed overlapping around agglomerated NPs. The *d*-spacing of CaO was little enhanced by the inclusion of dopants. Experimental outcomes indicated that the addition of Co-dopants improved the catalytic potential of CaO NPs. Al (4%)/St-doped CaO NPs expressed a significant reduction of methylene blue in a basic environment. The maximum bactericidal performance was observed as 10.25 mm and 4.95 mm in the inhibition zone against *S. aureus* and *E. coli*, respectively, after the addition of Al and St in CaO.

Received 8th October 2022
Accepted 28th October 2022

DOI: 10.1039/d2ra06340a

rsc.li/rsc-advances

1 Introduction

Water is an essential ingredient for many aspects of our lives, including growth and development, and its accessibility in its original form is crucial for all living things on the earth.[1,2] Although 71% of earth's crust is protected with water, hardly 0.03% is contemplated as fresh water that can be employed at firsthand.[3] The availability of purified and unpolluted water is affected by numerous factors with the elevated rate of population growth and the quick progress of industries.[2,4] Water is frequently contaminated with harmful compounds including different dyes, fertilizers, heavy metal ions, oil, and other unknown substances in industrial sectors of fabric, paper, food, and cosmetics.[5] Annually 1/10th million varieties of different dyes are produced from various textile industries, with MB accounting for 10–15% of the total. Industrial dyes and pollutants can cause major sickness in humans and animals, like cancer, skin sensitivities, allergies, or liver malfunction.[6] Over the last decade, a substantial burden on the dairy industry is mastitis, which is followed by somatic variation in the milk and irregularity of mammary gland function. Mastitis is attributable to species, namely, bacteria, fungi, and viruses.[7] *S. aureus* and *E. coli* are found to be common pathogenic bacteria causing a threat to human health.[8] Membrane separation, chemical oxidation, coagulation, flocculation, chemical precipitation, catalysis, photocatalysis, and adsorption processes were

[a]*Solar Cell Applications Research Lab, Department of Physics, Government College University Lahore, Lahore 54000, Punjab, Pakistan. E-mail: dr.muhammadikram@gcu.edu.pk*

[b]*Department of Clinical Sciences, Faculty of Veterinary and Animal Sciences, Muhammad Nawaz Shareef University of Agriculture, Multan, 66000, Punjab, Pakistan*

[c]*Department of Physics, RICAS, Riphah International University, Lahore 54000, Pakistan*

[d]*Core Research Facilities, King Fahd University of Petroleum & Minerals, Dhahran 31261, Saudi Arabia*

[e]*Tianjin Institute of Industrial Biotechnology, Chinese Academy of Sciences, Tianjin 300308, China*

[f]*Punjab University College of Pharmacy, University of the Punjab, Lahore, Pakistan*

[g]*Department d'Enginyeria Química, Universitat Rovira i Virgili, Tarragona 43007, Spain. E-mail: walid.nabgan@urv.cat*

[h]*College of Science, Physics Department, Alfaisal University, P.O. Box 50927, Riyadh 11533, Saudi Arabia*

[i]*Department of Physics, College of Science, King Faisal University, P.O. Box 400, Al-Ahsa, 31982, Saudi Arabia*

employed for removing heavy metals and dyes from water resources.[9–14] However, there are several limitations linked to these methodologies including incompetence, complicated and expensive procedure, elevated application and usage of a significant amount of energy.[2] Metal oxides including $ZnO{\cdot}Pr_6O_{11}$, La_2O_3, TiO_2, CdO, CeO_2, CaO, and Fe_2O_3, and zero-valent metals (ZVM) are frequently chosen as promising co-catalysts.[15] They can be used in several applications including efficient catalysis, medical diagnosis, and UV protection.[16] Among them, calcium oxide (CaO) is advantageous because of its non-poisonous nature, as well as low cost, extensive band gap energy (E_g), more stability, and higher catalytic activity (CA). The oxygen ion absorption is also enhanced using CaO, which is crucial for the catalysis process. CaO in bulk has a large E_g of 7.1 eV (ref. 17 and 18) and a high ε of 11.8 (dielectric constant). However, CaO has limitations such as large E_g and disability to utilize visible light in the degradation of dyes.[19–21] To overcome these limitations, various approaches have been adopted, which increase catalytic degradation as well as antibacterial action of CaO by doping polymers including St, acrylic binder, alginate, chitosan, and polyimide.[22] Recently, St has been proven to be an important industrial raw material that is utilized in different industries including foods, chemicals and medicines, as a fat substitute, water treatment agent and catalyst.[23,24] St is a naturally occurring biological macromolecule that acts as a catalyst for the elimination of dyes.[25] The CA of CaO can be further increased by doping group III members; Al-doped metal oxides exhibit less electrical resistance and good optical transmission in the visible region. However, we choose Al as a dopant.[26] In the present work, we adopted a co-precipitation approach to synthesize Al and St-doped CaO with different concentrations of Al (0, 2 and 4 wt%). The prepared products act as catalysts to remove the harmful dye MB. Its antibacterial action against different bacteria was also investigated.

2 Experimental section

2.1 Materials

Aluminum oxide (AL_2O_3), NaOH (98%), calcium chloride dihydrate ($CaCl_2{\cdot}2H_2O$, 99%), and starch ($(C_6H_{10}O_5)_n$, 99.6%) were acquired from Sigma-Aldrich. HCl (37%) was obtained from "Analar".

2.2 Synthesis of Al/starch-doped CaO

First, 0.5 M $CaCl_2{\cdot}2H_2O$ was utilized to synthesize CaO NPs by a co-precipitation approach under constant stirring at 90 °C. Afterwards, a desired amount of precipitating agent NaOH was added to obtain precipitates. Moreover, a colloidal solution was centrifuged two times at 7500 rpm for 6 min and heated overnight at 100 °C to get a fine powder. Similarly, to synthesize Al/St-doped CaO NPs, different concentrations of Al (2% and 4%) and St (5%) were prepared, as depicted in Fig. 1.

2.3 Catalytic activity

The reduction efficacy of dyes in the presence of $NaBH_4$ (reducing agent) and prepared catalysts was calculated through CA (Fig. 2). Using a quartz cell, 400 mL of $NaBH_4$ solution was combined with 3 mL MB. Adsorption appeared by incorporating 400 μL Al/St-doped CaO in the MB solution. The reaction rate

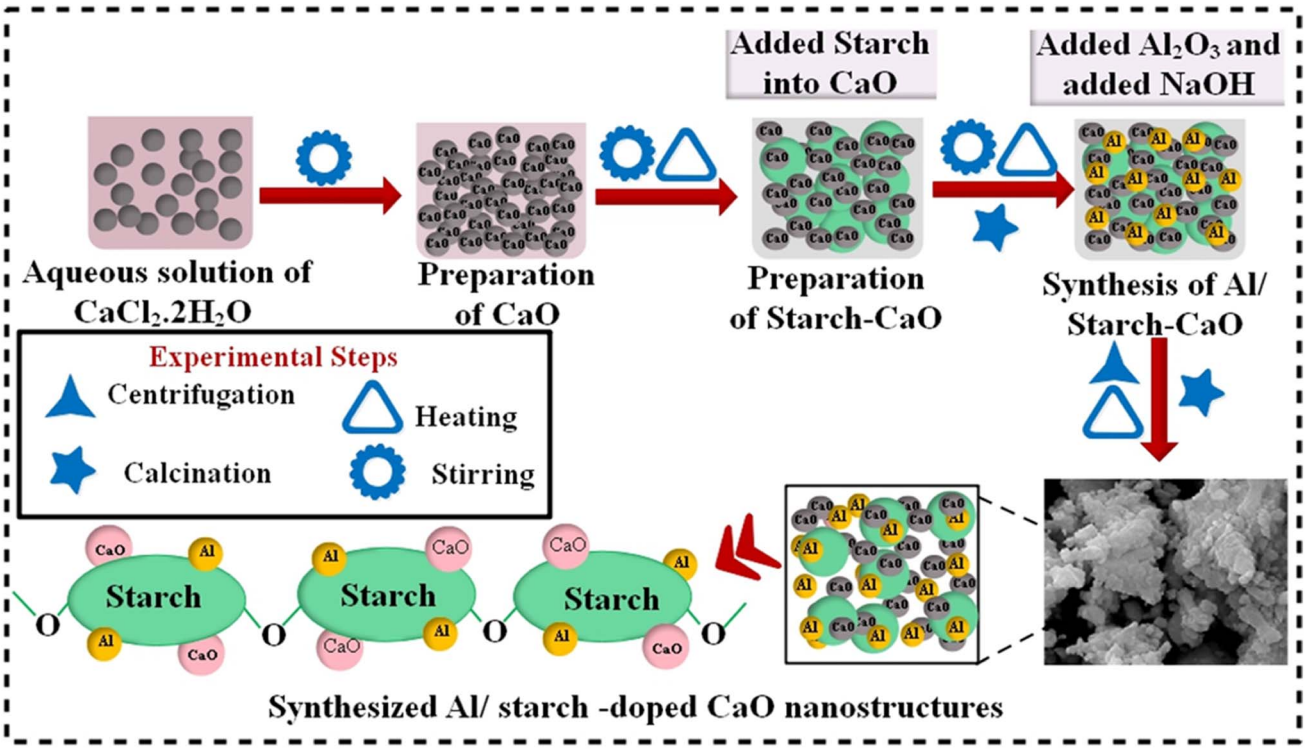

Fig. 1 Schematic diagram of the synthesis of Al/St-doped CaO NPs.

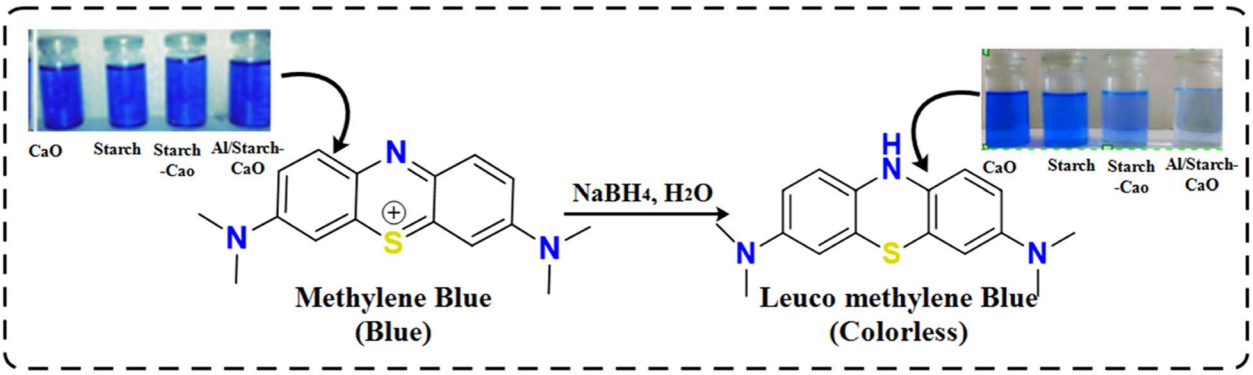

Fig. 2 Schematic diagram showing CA.

can be estimated by visualizing the decolorization and alteration in the intensity of dye consumption over time. The percentage degradation was calculated using the following formula:

$$\% \text{ Degradation} = (C_0 - C_t)/C_0 \times 100$$

During catalysis, the shifting of e^- from $NaBH_4$ to MB (oxidizing agent) promotes the redox reaction. The breakdown of MB occurred due to absorption of e^-. The degradation of MB in the presence of $NaBH_4$ is slow and time-consuming. The incorporation of catalysts in oxidation reduction reactions acts as an electron relay that shifts e^- from the donor (BH_4^-) to MB. The absorption of MB and BH_4^- ions increased in the presence of catalysts due to the large number of active sites allowing them to react quickly with each other causing a significant dye reduction efficacy.

2.4 Segregation and characterization of *S. aureus* and *E. coli*

Mastitis was accumulated from animal hospitals in Punjab, Pakistan, swabbed at 5% sheep blood agar for initial culturing. Overnight development at 37 °C continued and generated bacteria were refined by streaking on mannitol salt agar (MSA) and MacConkey agar (MA) in triplicate.

Isolated colonies were recognized by biochemical tests (catalase and coagulase) and topographically using the gram staining.

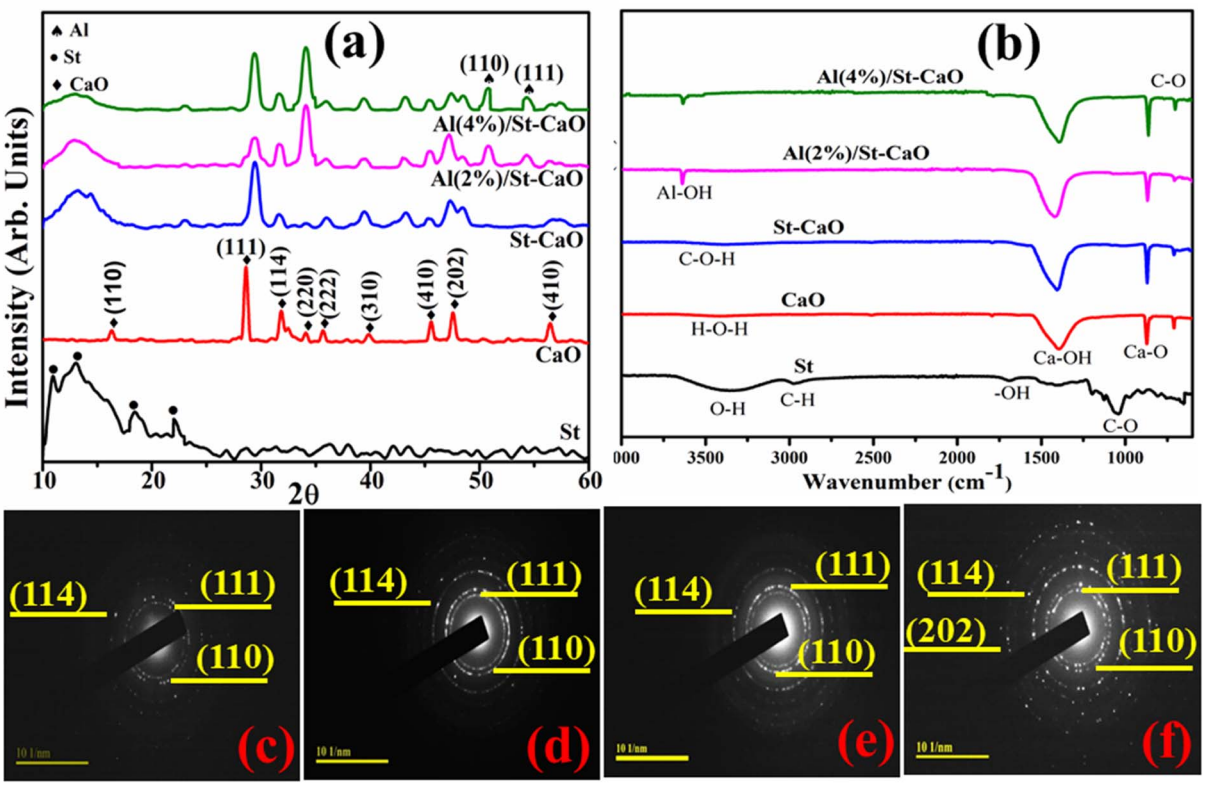

Fig. 3 (a) XRD spectra, (b) FTIR analysis of prepared samples and (c–f) SAED pattern of CaO, St/CaO, and Al (2 and 4%)/St-CaO.

2.5 Antimicrobial activity

The *in vitro* antimicrobial activity of Al and St-doped CaO proceeded by adopting an agar well diffusion method on isolated Gram +ve and Gram −ve microbes. Different concentrations of Al/St-doped CaO (0.5 mg and 1.0 mg/50 μL) associated with less and high doses, respectively, were tipped into a 6 mm – wide well that is made by utilizing a sterile cork borer. Ciprofloxacin (5 μg/50 μL) was employed as a +ve control, while DIW (50 μL) was designated a −ve control. The antibacterial performances of all generated products were measured using a vernier caliper after the incubation of Petri dishes at 37 °C for 12 h. One-way analysis of variance was employed to evaluate the antibacterial effects of Al/St-doped CaO.

3 Results and discussion

XRD technique was applied on pristine CaO and Al/St-doped CaO in the 2θ range of 10–60° to investigate the crystallite size, phase constitution, and crystal structure, as demonstrated in Fig. 3(a). The observed reflection peaks located at ~28.4159°, 31.7182°, 35.83°, 39.53°, 47.24° and 56.49° were assigned to the (111), (114), (222), (310), (202), and (410) facets, respectively. These crystallographic facet corresponds to the cubic structure of CaO associated with the standard spectrum (ICDD card no. 00-7017-0912) along with the space group $Fm\bar{3}m$.[27] Additional peaks sited at $2\theta = 16.41°$ (110), 34.22° (220), and 45.51° (410) correspond to the hexagonal phase of $CaCO_3$ (H_2O) along with the space group P31 (JCPDS no. 083-1923). These peaks are attributed to the carbonic nature of calcite ($CaCO_3$) owing to trigger by the carbonic reaction of $Ca(OH)_2$ in which its generation stems from the hydration of clinker minerals.[28] St was ascribed to peaks at 10.95°, 13.02°, 18.08°, 22.99° and 43.01°.[29,30] Upon Al doping, extra peaks were observed at 50.9° (110) and 54.3° (111), which correspond to the tetragonal structure of Al_2O_3 (JCPDS card no. 016-0494).[31] These supplementary peaks justified the presence of crystalline Al particles on the CaO surface. Peaks became broad with the increase in the doping ion concentration (St and Al), which could be attributed to the lattice strain in the samples. The broadening of the diffraction peak can be due to the small nanosize of the crystalline sample, strain, and instrumental factors.[3,32] The average crystallite sizes were determined from line broadening using the Scherer formula and, as a result, the crystallite sizes were 11, 26.03, 25.72 and 30.02 nm for CaO, St-CaO, and Al (2, 4%)/St-CaO. The existence of the functional group and chemical bond formation of pure and Al/St-doped CaO were assessed with the FTIR spectra, as illustrated in Fig. 3(b). Due to the Al–OH group stretching vibration, a large band appeared at around

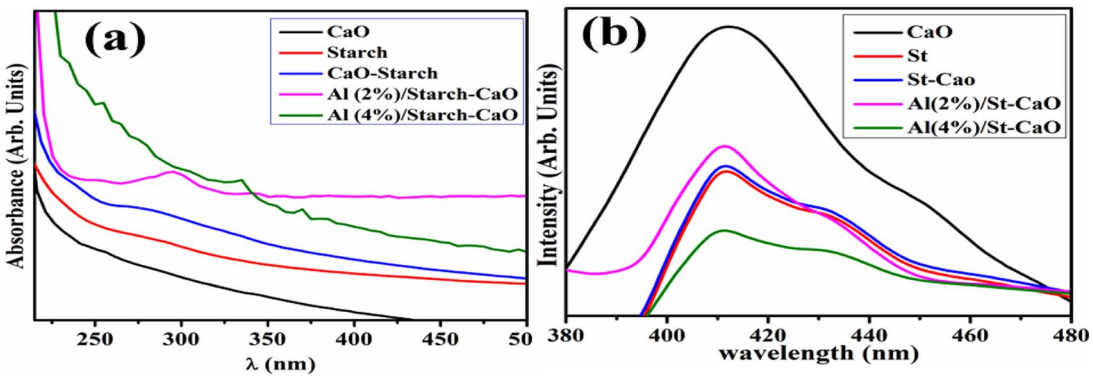

Fig. 4 (a) UV-vis spectra and (b) PL spectra of CaO, St, St/CaO, and Al (2 and 4%)/St-CaO.

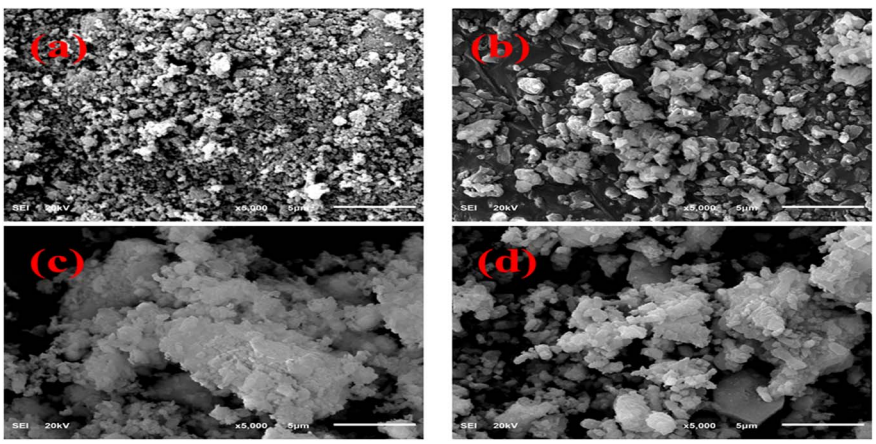

Fig. 5 FESEM images of (a) CaO, (b) St-CaO, (c) Al (2%)/St-CaO and (d) Al (4%)/St-CaO.

3639 cm^{-1}.[33] The band at 3434 cm^{-1} was assigned to the H–O–H bending vibration caused by adsorbed water molecules.[34] The bands at 1411, 864, and 702 cm^{-1} represented the Ca–OH, Ca–O, and C–O stretching vibration, correspondingly,[35] which indicates the presence of CaO. However, common signals are depicted in the St spectrum, such as bands at 3372, 2975, 1664, 1066 and 702 cm^{-1} corresponding to the O–H, C–H, –OH, and C–O stretching vibrations respectively.[35,36] The SAED pattern displayed distinct rings associated with different planes, *i.e.*, (111), (110), (114), and (202) of primeval and doped samples, as demonstrated in Fig. 3(c–f). These results confirming the crystalline material matched well with the XRD data.

The optical characteristics of dopant-free and Al/St-doped CaO were examined through the UV-vis absorption spectra

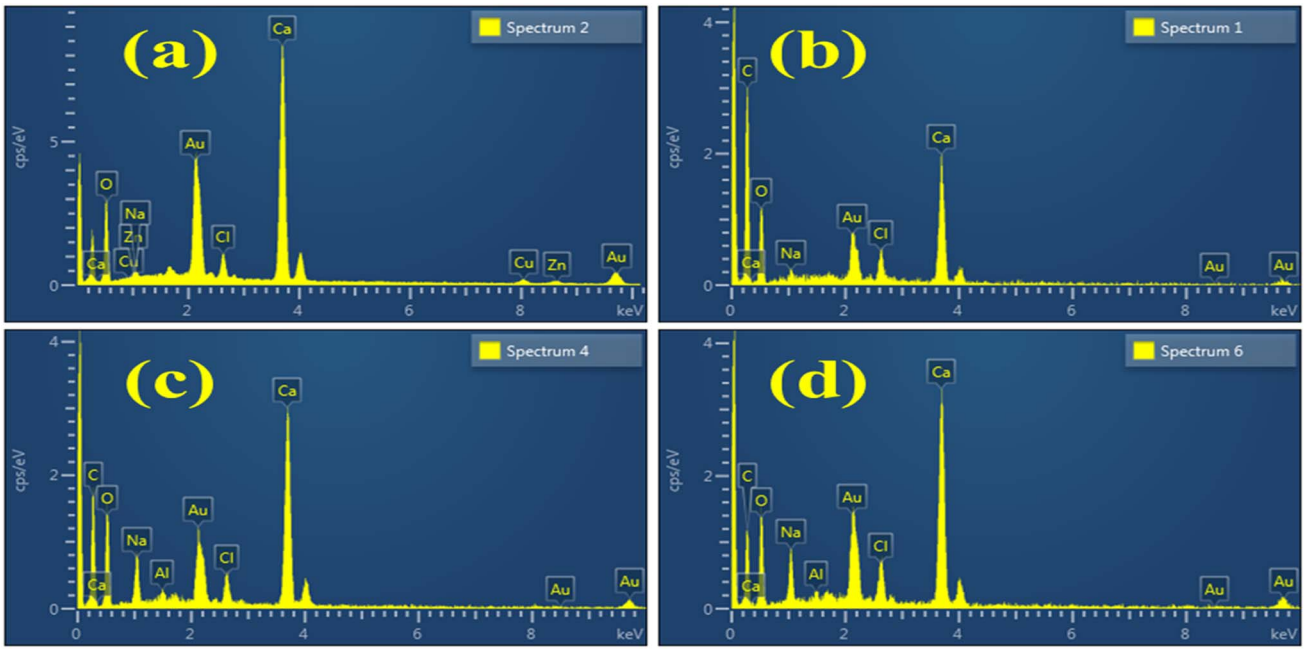

Fig. 6 EDS analysis of (a) CaO, (b) St-CaO, (c) Al (2%)/St-CaO and (d) Al (4%)/St-CaO.

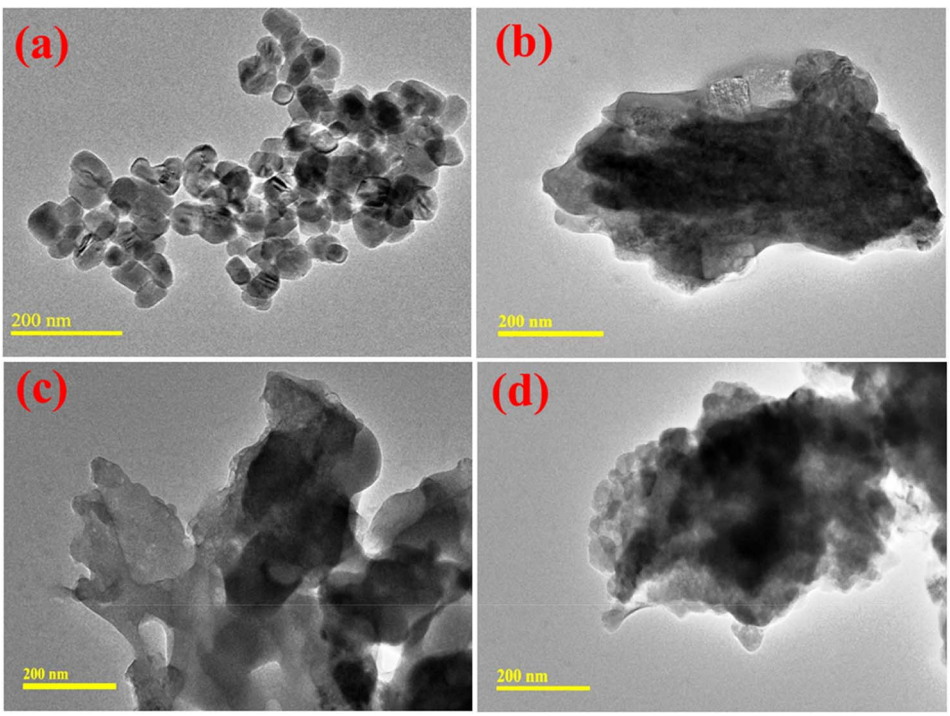

Fig. 7 HR-TEM image of (a) CaO, (b) St-CaO, (c) Al (2%)/St-CaO and (d) Al (4%)/St-CaO.

displayed (220–450 nm) in Fig. 4(a). The highest absorption peak of CaO was detected at 250 nm, which was attributed to the transfer of an electron from the 2p to 4s state of the VB of O^{2-} to the CB of Ca^{2+}, respectively,[37] and the absorption peak of St was sited at 255 nm.[38] The E_g values were calculated from the UV-vis spectra, and direct E_g was found to be 4.94,[39] 4.86, 4.45, 4.28, and 4.13 eV for CaO, St, St-CaO, 2% Al/St-doped CaO and 4% Al/St-doped CaO, respectively. Furthermore, with the addition of St and Al (2, 4)%, the absorption peak was moved to a higher wavelength and a redshift assigned to the quantum confinement effect was detected.[40] The PL spectra displayed the charge carrier movement and electron–hole recombination ability. The PL emission spectra of pure Al/St and doped CaO NPs were recorded from 370 to 480 nm at an excitation wavelength of 350 nm, as illustrated in Fig. 4(b). The emission peak of CaO and St was observed at 411 nm, which exhibited the direct transition (band-to-band) produced by an electron–hole recombination that occurred at different E_g regions.[41] Additionally, when Al and St were added to a pure material, a slight blue-shift to 409 nm occurred and the intensity decreased in contrast to CaO. The decrease in the PL intensity of Al/St-doped CaO is attributed to the minimum exciton recombination, which is suitable for CA.[42–44]

The FESEM technique was used to analyze the morphology of primeval and doped CaO. The pure sample revealed the random distribution, non-uniform and polycrystalline morphology of particles, as demonstrated in Fig. 5(a). The particles scattered and increased in size with the addition of St, as shown in Fig. 5(b). Upon the addition of Al, a higher level of agglomeration of non-homogenous particles was observed and this trend increased with the increasing amount of Al, as illustrated in Fig. 5(c and d).

EDS analysis examined the weight percentage of various elements contained in Al/St-CaO NPs. The presence of Ca and O peaks confirmed the synthesis of CaO, as shown in Fig. 6(a). The spectra of doped materials are nearly similar to that of the pure material, excluding the peaks of C attributed to the doping of St, as shown in Fig. 6(b). In Fig. 6(c and d), the Al peak shows dopant incorporation. Due to the gold coating sputtering over the sample to reduce the charging effect, an Au peak was detected in the spectra.[45] Additional peaks of Na found in the spectra were assigned to the NaOH solution, which was used to adjust the pH during the synthesis of materials.[46]

HR-TEM analysis was undertaken to determine the morphological characteristics of the prepared nanocatalysts. In Fig. 7(a), the HR-TEM micrographs demonstrate the formation

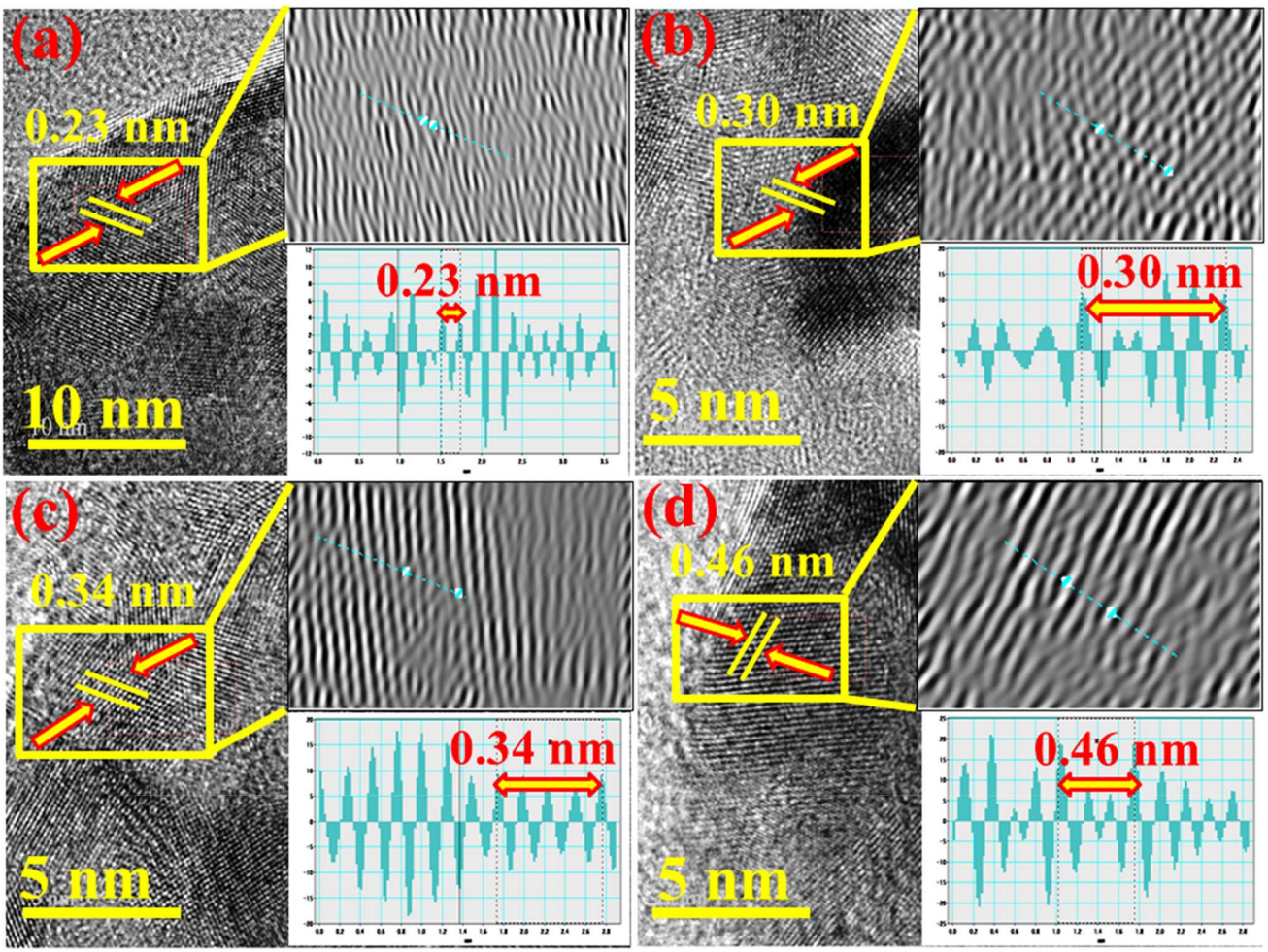

Fig. 8 *d*-spacing of (a) CaO, (b) St-CaO, (c) Al (2%)/St-CaO and (d) Al (4%)/St-CaO.

of regular cubic-shaped NPs. After that, the incorporation of St showed overlapping around agglomerated NPs, as shown in Fig. 7(b). The higher degree of agglomeration of NPs was observed by Al doping. This pattern was increased by a higher concentration of Al that confirmed the partial interaction between Al and CaO NPs, as demonstrated in Fig. 7(c and d).

The *d*-spacing of pristine and Al/St-doped CaO was determined using the HR-TEM image at a higher magnification up to 5–10 nm. The calculated *d*-spacing of CaO was ~0.23 nm, which correlated with the (310) facet of XRD, as illustrated in Fig. 8(a). Upon St and Al doping, the *d*-spacing was slightly increased to ~0.30, 0.34, and 0.46 nm, which is in accordance with the XRD results, as elaborated in Fig. 8(b–d).

The XRD spectra revealed the cubic structure of CaO NPs and no significant changes occurred upon doping of St and Al. The crystallite size was enhanced from 11 to 30.02 nm upon doping. The UV-vis spectra exhibited a red-shift upon doping and E_g was also decreased. The HR-TEM image displayed the formation of cubic-shaped NPs of CaO and agglomeration was observed by the addition of St and Al.

The dye elimination of MB during CA of pristine and Al/St-doped CaO was investigated by utilizing $NaBH_4$ as a reducing agent. The maximum degradation of pure and doped samples

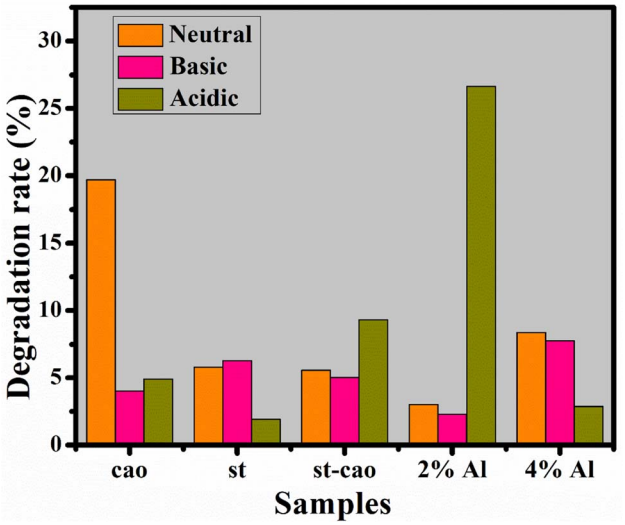

Fig. 10 Catalysis of CaO, St, St/CaO, and Al (2 and 4%)/St-CaO in neutral, basic and acidic media in terms of rate degradation (%).

was 78.88–92.71% in a neutral medium, 72.48–93.21% in a basic medium, and 73.79–86.17% in an acidic medium found statistically significant ($P < 0.05$), as illustrated in Fig. 9(a–c). The

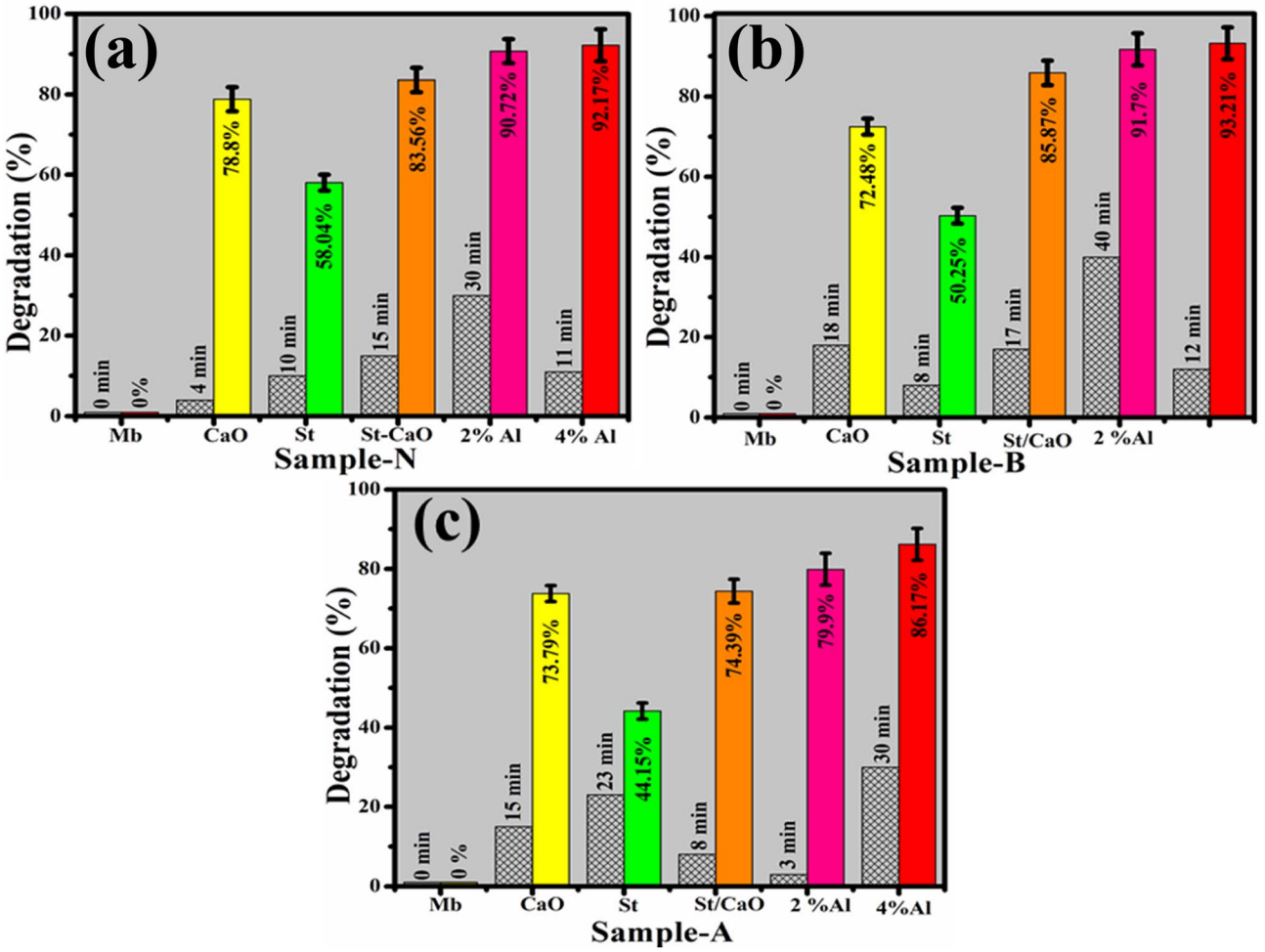

Fig. 9 Catalysis of CaO, St, St/CaO, Al (2 and 4%)/St-CaO in (a) neutral, (b) basic and (c) acidic media in terms of percentage degradation.

largest CA was obtained with 4 percent Al/St-doped CaO in all media in terms of percentage degradation. The crystallinity, structure, and surface area of NPs all affect CA. During CA, the reduction of MB occurs in the existence of $NaBH_4$, and synthesized catalysts operate as electron relays that shift electrons from BH_4^- ions to MB ensuring the dye reduction. The nanostructure having plenteous active sites elevates the BH_4^- ion and dye molecules. Generally, a catalyst associated with a large surface area possesses a high CA owing to the delivery of more active sites to react with each other.[47,48] The pH of the synthesized solution has a significant impact on degradation efficiency. The increased generation of H^+ ions accessible to be captivated on the NP surface was attributable to improved CA in the acidic medium. The large number of OH^- in the basic medium (NaOH) cause the oxidation of reduced products and lower the CA.[47,49,50]

If CA is considered in terms of degradation rate, then 2% Al/St-doped CaO NPs exhibit the best catalytic behavior in the acidic environment, as elaborated in Fig. 10.

The degradation rate can be calculated as follows:

$$\%\ \text{Degradation rate} = \frac{(C_0 - C_t)/C_0}{t} \times 100$$

Fig. 11 represents the antibacterial action of pure and Al/St-doped CaO against *S. aureus* and *E. coli* by the agar well diffusion method, which is summarized in Table 1. For Al/St-doped CaO, the significant inhibition result of *S. aureus* was obtained to be 1.35–6.45 mm and 2.25–10.25 mm, and similarly, 0–3.45) and (1–4.95 mm for *E. coli* at both doses. The consequences of inhibition zones of bacteria were compared by utilizing the −ve control DIW (0 mm) and +ve control ciprofloxacin (11.30 mm) and (5.35 mm), for *S. aureus* and *E. coli* respectively compared with DIW (0 mm). The results indicated that bare and Al/St-doped CaO NPs showed high performance

Table 1 Antimicrobial activity of pure and Al/St-doped CaO NPs

	Inhibition areas[a] (mm)		Inhibition areas[b] (mm)	
Samples	0.5 mg/50 μL	1 mg/50 μL	0.5 mg/50 μL	1 mg/50 μL
CaO	0	1.05	0	0.6
St/CaO	1.35	2.25	0	1
Al (2%)	5.80	7.35	1.25	1.40
Al (4%)	6.45	10.25	3.45	4.95
Ciprofloxacin	11.30	11.30	5.35	5.35
DIW	0	0	0	0

[a] Inhibition zones (mm) Al/St doped CaO for *S. aureus*. [b] Inhibition area (mm) measurement of Al/St doped CaO for *E. coli*.

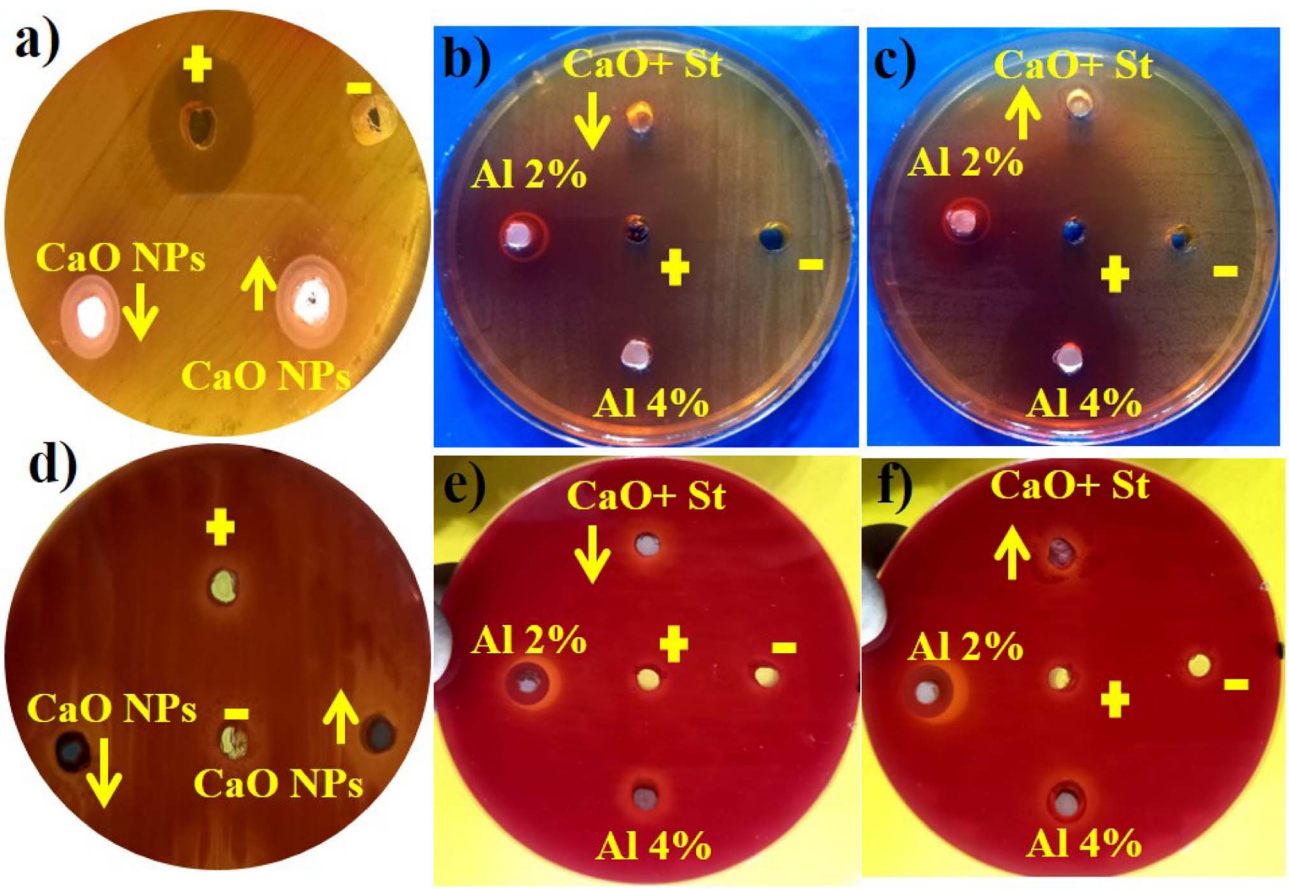

Fig. 11 Antibacterial activity of the synthesized samples against (a–c) *S. aureus* at high and low doses and (d–f) *E. coli* at maximal and minimal doses.

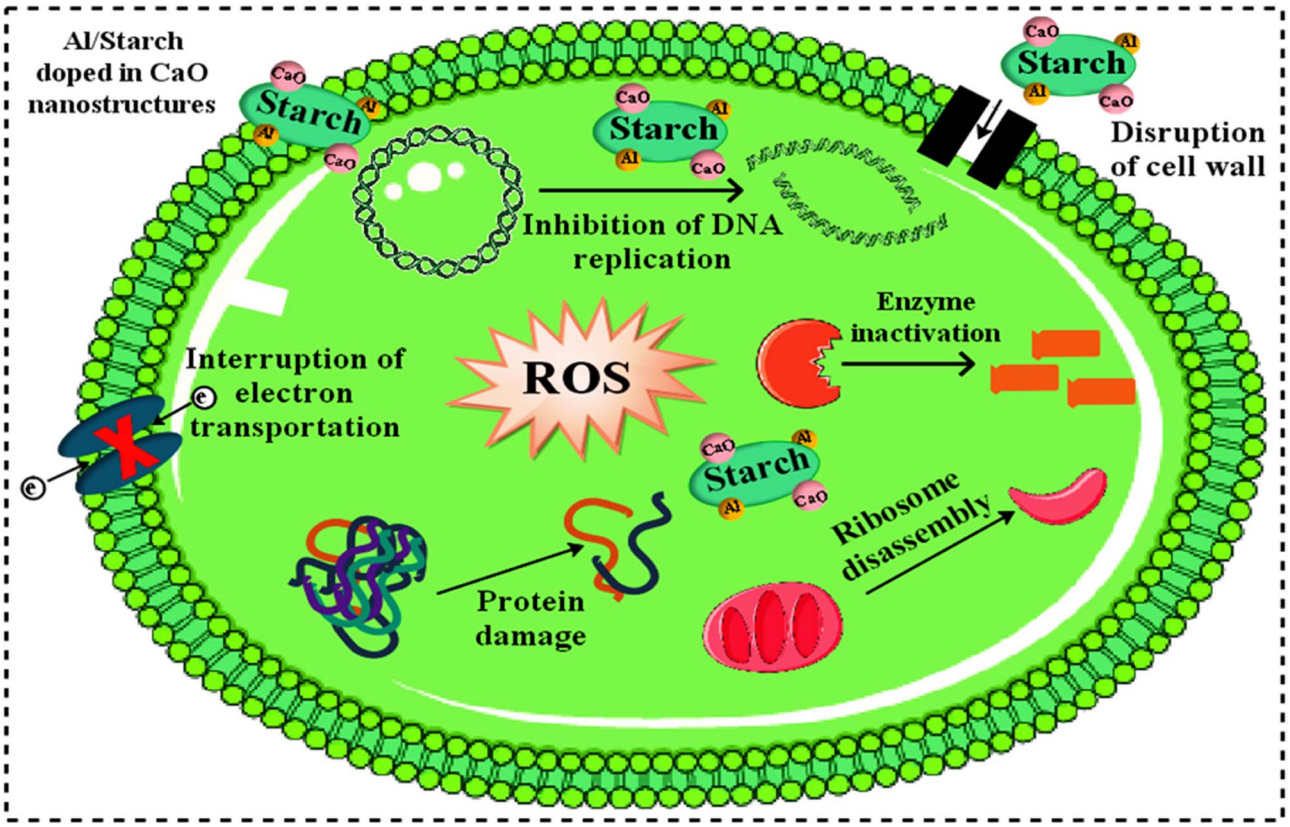

Fig. 12 Antibacterial mechanism of Al/St-doped CaO NPs.

Table 2 Literature comparison of catalysis and antibacterial activity of 4% Al/St-doped CaO NPs

Materials	Synthesis route	Catalytic activity	Antimicrobial activity	Ref.
Cao NPs	Co-precipitation	72.2%	2.25 mm and 3.30 mm against *E. coli* and *S. aureus* respectively	52
Ag/CaO nanocomposite	Green synthesis	70%	6.30 mm and 9.15 mm against *E. coli* and *S. aureus* respectively	53
CaO NPs	Green syntheses	—	6 mm against *E. coli*	54
CaO nano flowers	Green synthesis	76%	—	55
CaO NPs	Co-precipitation	70.64%	3.30 mm and 2.25 mm against *E. coli* and *S. aureus* respectively	56
4% Al/St doped CaO NPs	Co-precipitation	93.21%	10.25 mm and 4.95 m against *E. coli* and *S. aureus* respectively	Present study

against G +ve compared to G −ve bacteria. The antibacterial activity of CaO NPs could be assigned to different factors such as connections with OH^- and H_2O existence at the surface, which generates the reactive oxygen species (ROS), as shown in Fig. 12. ROS spread around the bacteria, resulting in protruding cytoplasmic components, thereby killing the bacteria.[51] The contrast of current work with the literature is depicted in Table 2.

To gain an in-depth understanding of St/Al-doped CaO, the calculations reported mainly depend upon the density functional theory (DFT) performed using the Quantum Atomistix ToolKit (QuantumATK) computer code.[57] Throughout the calculations, the local combination of atomic orbitals (LCAO) method and the generalized gradient approximation (GGA) using the Perdew–Burke–Ernzerhof (PBE) method[58] were used. The PseudoDojo-medium norm-conserving pseudopotential[59] and a cut-off energy of 10^5 Ha were considered for simulation. The Brillouin region was sampled using a $7 \times 7 \times 1$ k-point mesh produced by the Monkhorst–Pack grid method. The density of states (DOS) was computed using a more accurate Heyd–Scuseria–Ernzerhof (HSE06) functional.[60,61] The optimized lattice constant of bulk cubic CaO was found to be $a =$ 4.839 Å, which matches well with the experimental values ($a =$ 4.8105 Å).[62] Periodic slabs with a p (4×4) lateral cell having a thickness of four atomic layers and a vacuum gap of 15 Å in the direction perpendicular to the surface were used to model the CaO (001) surface of the optimized bulk structure, as shown in Fig. 6(a). Because the CaO (001) surface is the most stable surface, it was chosen as the model for simulating St adsorption.[63] To examine the interactions between St and CaO, we calculated the St Adsorption on the CaO surface and St/Al-doped CaO surface. The adsorption energy was calculated using the following expression:[64,65] $E_{ads} = E_{(molecule+slab)} - Es_{lab} - E_{molecule}$, where $E_{molecule+slab}$, E_{slab}, and $E_{molecule}$ denote the total energies

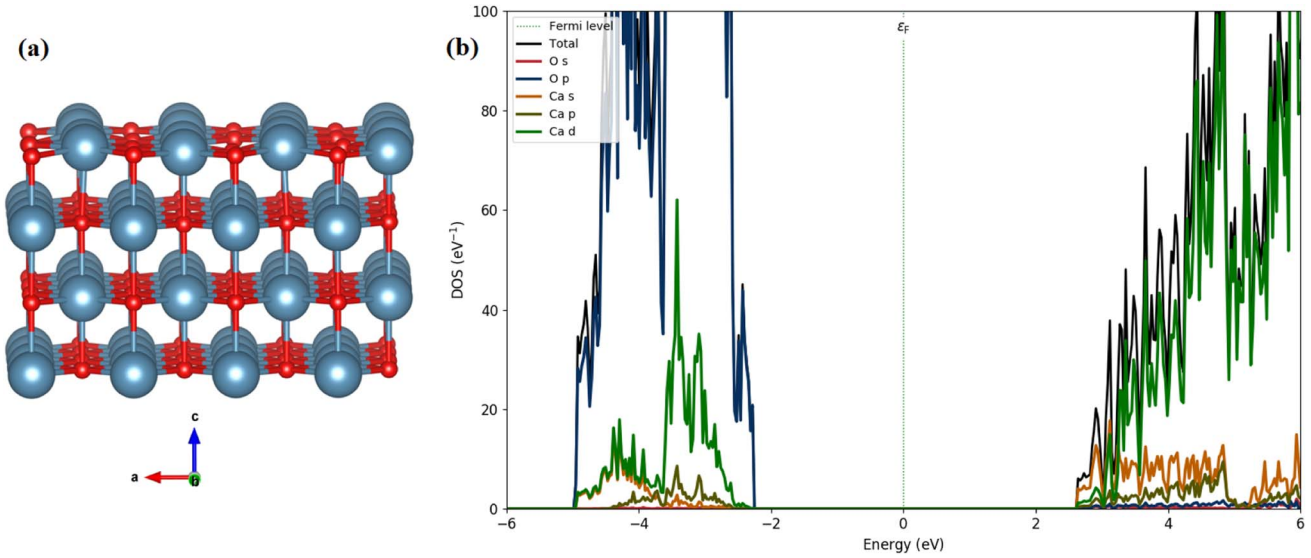

Fig. 13 Optimized structures (a) side view (red: O; cyan: Ca), and (b) the calculated DOSs of the CaO (001) surface.

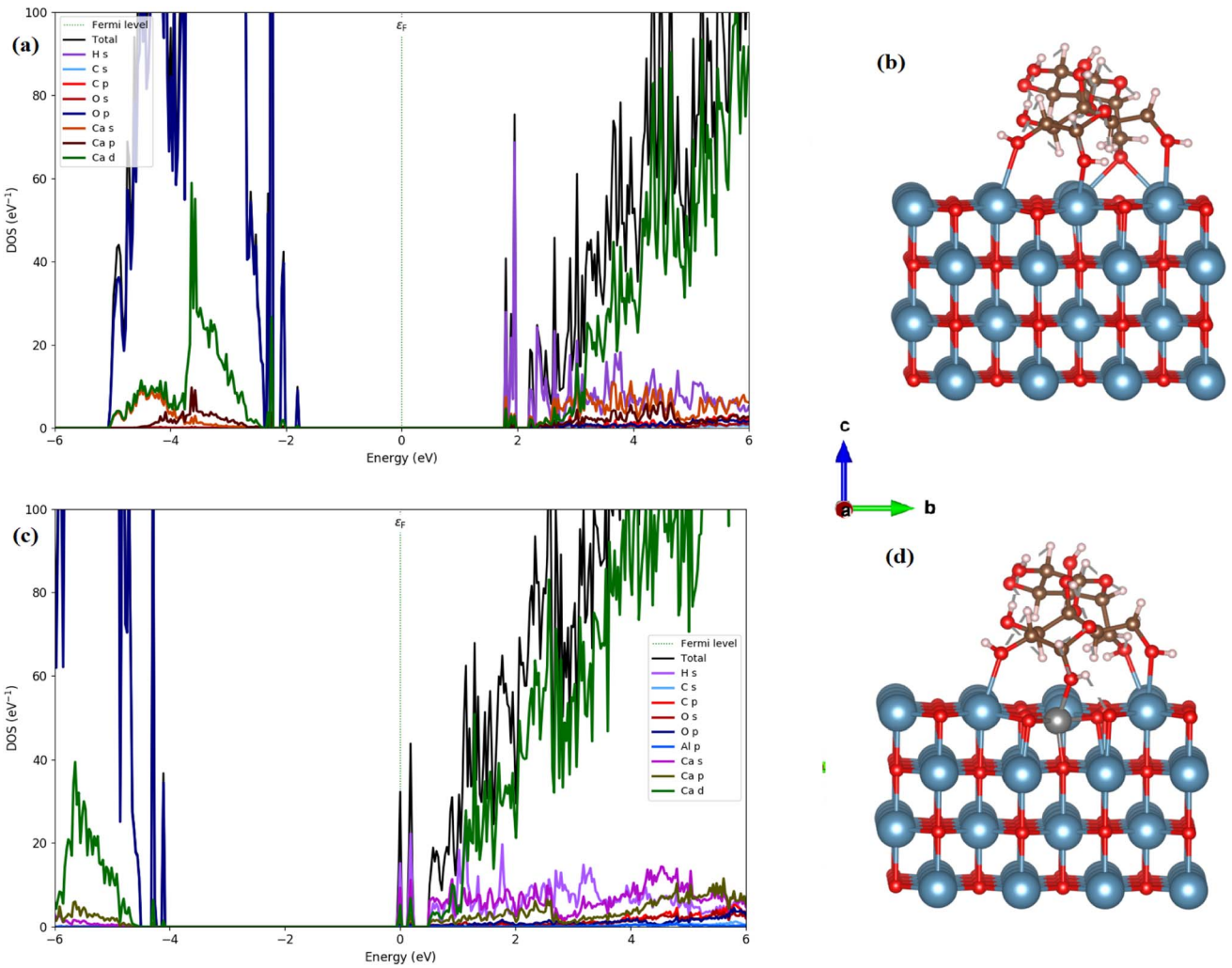

Fig. 14 Total and partial DOS and schematic of the slab model of (a) and (b) St on the CaO (001) surface and (c) and (d) Al/St on the CaO (001) surface. (cyan: Ca; red: O; silver: Al; brown: C; light blue: N; gray: H).

of the St-CaO (001) and St/Al-CaO (001) complexes, pure surface, and the isolated gas molecule, respectively. The calculated E_{ads} values of −0.98 eV and −0.93 eV with respect to St on the CaO (001) surface and St/Al-CaO (001) surface systems show endothermic adsorption energy. The bond distance of O in St–Ca is 2.360 Å for the St-CaO (001) surface. Meanwhile, the bond distance of O in starch-Ca decreased to 2.280 Å in the St/Al-CaO (001) surface system.

We calculated the total and partial density of states (DOS) using the HSE06 functional, as illustrated in Fig. 13(b). The calculated band gap of 3.45 eV for CaO (001) is consistent with our experimental measurements (4.94 eV). The analysis of the PDOS plot (Fig. 13(b)) reveals that the significant contribution to the valence band maximum (VBM) comes from O 2p states (see Fig. 13(a)). However, the unoccupied conduction band minimum (CBM) is mainly constructed by the unoccupied Ca 4s states with a contribution of Ca 3d and 3 p states.

We, therefore, performed the electronic calculations on starch on the CaO (001) and St/Al-CaO (001) surfaces by investigating the total and partial DOS, as shown in Fig. 14. For St on CaO (001), the band structure shows that flat bands are formed near the edge of valence and conduction bands. It was found that St on CaO (001) induced the in-gap state near CBM mainly due to the H s states, whereas O 2p orbitals mainly construct the flat band near VBM. A more interesting point noticed here is that the bandgap decreases at a value of 3.55 eV. Al doping in the St-CaO (001) complex follows the DOS plots that the conduction and valence band edges are shifted to lower energies. Moreover, a similar feature is observed in electronic structures.

4 Conclusion

Al/St-doped CaO NPs have been successfully synthesized by a co-precipitation approach and found to be efficient in reducing dyes from polluted water. The XRD spectra confirmed the cubic structure of CaO, and no variations occurred in the cubic phase by doping of St and Al. The crystallite size was enhanced from 11 to 30.02 nm upon doping. Moreover, the band gap energy was reduced as the Al concentration in the starch-doped CaO system was raised, according to the hybrid density functional investigation. The addition of co-dopants to the optical absorption spectra of the synthesized materials exhibited a redshift in the absorption spectra. Moreover, the E_g value of CaO NPs was reduced by St and Al doping. TEM exhibited the formation of cubic-shaped NPs of CaO by a co-precipitation method. EDS spectra revealed the elemental composition and successful incorporation of dopants. Al (4%)/St-CaO NPs exhibited a maximum degradation of 93.21% in a basic media compared to the pure material. Obtainable samples demonstrated statistically significant outcomes against *S. aureus* at minimum and maximum concentrations with a diameter ranging from 1.35 to 6.45 mm and 2.25 to 10.25 mm, respectively. *E. coli* had the least resistance and the most significant findings from diameters ranging from 0 to 3.45 and 1 to 4.95 mm for the minimum and maximum concentrations, respectively. Al/St-doped CaO NPs (2% and 4%) have shown higher antibacterial activities against *E. coli* than against *S. aureus*.

Author contributions

Muhammad Ikram: conceptualization, supervision, Ali Haider: investigation, data curation, Syeda Tayaba Bibi: writing – original draft, Anwar Ul-Hamid: methodology, Junaid Haider: methodology, Iram Shahzadi: writing – original draft, Walid Nabgan: project administration, Sawaira Moeen: writing – original draft, Salamat Ali: resources, souraya Goumri-said: software, Benali Kanoun: formal analysis.

Conflicts of interest

The authors declare no conflict of interest.

Acknowledgements

Authors are grateful to HEC, Pakistan, for financial support through NRPU-20-17615.

References

1 M. K. Daud, M. Nafees, S. Ali, M. Rizwan, R. A. Bajwa, M. B. Shakoor, M. U. Arshad, S. A. S. Chatha, F. Deeba, W. Murad, I. Malook and S. J. Zhu, Drinking Water Quality Status and Contamination in Pakistan, *Biomed Res. Int.*, 2017, **2017**, 7908183, DOI: **10.1155/2017/7908183**.

2 M. Ikram, A. Raza, M. Imran, A. Ul-Hamid, A. Shahbaz and S. Ali, Hydrothermal Synthesis of Silver Decorated Reduced Graphene Oxide (rGO) Nanoflakes with Effective Photocatalytic Activity for Wastewater Treatment, *Nanoscale Res. Lett.*, 2020, **15**, 95, DOI: **10.1186/s11671-020-03323-y**.

3 A. Ahmad, S. H. Mohd-Setapar, C. S. Chuong, A. Khatoon, W. A. Wani, R. Kumar and M. Rafatullah, Recent advances in new generation dye removal technologies: novel search for approaches to reprocess wastewater, *RSC Adv.*, 2015, **5**, 30801–30818, DOI: **10.1039/c4ra16959j**.

4 S. Dervin, D. D. Dionysiou and S. C. Pillai, 2D nanostructures for water purification: Graphene and beyond, *Nanoscale*, 2016, **8**, 15115–15131, DOI: **10.1039/c6nr04508a**.

5 M. Sharma, K. Behl, S. Nigam and M. Joshi, TiO2-GO nanocomposite for photocatalysis and environmental applications: A green synthesis approach, *Vacuum*, 2018, **156**, 434–439, DOI: **10.1016/j.vacuum.2018.08.009**.

6 S. A. Khan, Z. Arshad, S. Shahid, I. Arshad, K. Rizwan, M. Sher and U. Fatima, Synthesis of TiO2/Graphene oxide nanocomposites for their enhanced photocatalytic activity against methylene blue dye and ciprofloxacin, *Compos. Part B Eng.*, 2019, **175**, 107120, DOI: **10.1016/j.compositesb.2019.107120**.

7 N. J. Vickers, Animal Communication: When I'm Calling You, Will You Answer Too?, *Curr. Biol.*, 2017, **27**, R713–R715, DOI: **10.1016/j.cub.2017.05.064**.

8 D. Manyasree, P. Kiranmanyi and R. V. S. S. N. Ravi Kumar, Synthesis, characterization and antibacterial activity of

aluminium oxide nanoparticles, *Int. J. Pharm. Pharm. Sci.*, 2018, **10**, 32, DOI: 10.22159/ijpps.2018v10i1.20636.

9 L. Zhu, L. Zong, X. Wu, M. Li, H. Wang, J. You and C. Li, Shapeable Fibrous Aerogels of Metal-Organic-Frameworks Templated with Nanocellulose for Rapid and Large-Capacity Adsorption, *ACS Nano*, 2018, **12**, 4462–4468, DOI: 10.1021/acsnano.8b00566.

10 S. Sadri Moghaddam, M. R. Alavi Moghaddam and M. Arami, Coagulation/flocculation process for dye removal using sludge from water treatment plant: Optimization through response surface methodology, *J. Hazard. Mater.*, 2010, **175**, 651–657, DOI: 10.1016/j.jhazmat.2009.10.058.

11 E. M. Siedlecka, A. Ofiarska, A. F. Borzyszkowska, A. Białk-Bielińska, P. Stepnowski and A. Pieczyńska, Cytostatic drug removal using electrochemical oxidation with BDD electrode: Degradation pathway and toxicity, *Water Res.*, 2018, **144**, 235–245, DOI: 10.1016/j.watres.2018.07.035.

12 H. Fan, J. Gu, H. Meng, A. Knebel and J. Caro, High-Flux Membranes Based on the Covalent Organic Framework COF-LZU1 for Selective Dye Separation by Nanofiltration, *Angew. Chemie - Int. Ed.*, 2018, **57**, 4083–4087, DOI: 10.1002/anie.201712816.

13 R. Biczak, B. Pawłowska, P. Bałczewski and P. Rychter, The role of the anion in the toxicity of imidazolium ionic liquids, *J. Hazard. Mater.*, 2014, **274**, 181–190, DOI: 10.1016/j.jhazmat.2014.03.021.

14 M. Ali, A. Sarkar, M. D. Pandey and S. Pandey, Efficient precipitation of dyes from dilute aqueous solutions of ionic liquids, *Anal. Sci.*, 2006, **22**, 1051–1053, DOI: 10.2116/analsci.22.1051.

15 K. Kaviyarasu, P. P. Murmu, J. Kennedy, F. T. Thema, D. Letsholathebe, L. Kotsedi and M. Maaza, Structural, optical and magnetic investigation of Gd implanted CeO2 nanocrystals, *Nucl. Instrum. Methods Phys. Res., Sect. B*, 2017, **409**, 147–152, DOI: 10.1016/j.nimb.2017.02.055.

16 E. K. Goharshadi, S. Samiee and P. Nancarrow, Fabrication of cerium oxide nanoparticles: Characterization and optical properties, *J. Colloid Interface Sci.*, 2011, **356**, 473–480, DOI: 10.1016/j.jcis.2011.01.063.

17 R. C. Whited, C. J. Flaten and W. C. Walker, Exciton thermoreflectance of MgO and CaO, *Solid State Commun.*, 1973, **13**, 1903–1905, DOI: 10.1016/0038-1098(73)90754-0.

18 J. Osuntokun, D. C. Onwudiwe and E. E. Ebenso, Aqueous extract of broccoli mediated synthesis of CaO nanoparticles and its application in the photocatalytic degradation of bromocrescol green, *IET Nanobiotechnol.*, 2018, **12**, 888–894, DOI: 10.1049/iet-nbt.2017.0277.

19 M. A. Bolorizadeh, V. A. Sashin, A. S. Kheifets and M. J. Ford, Electronic band structure of calcium oxide, *J. Electron Spectros. Relat. Phenomena.*, 2004, **141**, 27–38, DOI: 10.1016/j.elspec.2004.04.004.

20 E. L. Albuquerque and M. S. Vasconcelos, Structural, electronics and optical properties of CaO, *J. Phys.: Conf. Ser.*, 2008, 42006, DOI: 10.1088/1742-6596/100/4/042006.

21 M. A. Aseel, F. H. Itab and F. M. Ahmed, Producing High Purity of Metal Oxide Nano Structural Using Simple Chemical Method, *J. Phys. Conf. Ser.*, 2018, 12036, DOI: 10.1088/1742-6596/1032/1/012036.

22 J. Ma, W. Zhu, Y. Tian and Z. Wang, Preparation of Zinc Oxide-Starch Nanocomposite and Its Application on Coating, *Nanoscale Res. Lett.*, 2016, **11**, 200, DOI: 10.1186/s11671-016-1404-y.

23 T. Cai, H. Lin, Z. Liu, K. Chen, Y. Lin, Y. Xi and K. Chhuond, Starch wastewater treatment technology, *IOP Conf. Ser. Earth Environ. Sci.*, 2019, 22054, DOI: 10.1088/1755-1315/358/2/022054.

24 Q. Chen, H. Yu, L. Wang, Z. Ul Abdin, Y. Chen, J. Wang, W. Zhou, X. Yang, R. U. Khan, H. Zhang and X. Chen, Recent progress in chemical modification of starch and its applications, *RSC Adv.*, 2015, **5**, 67459–67474, DOI: 10.1039/c5ra10849g.

25 F. Zhang, X. Pei, K. Zhai, C. Wang, Y. Bai, B. Zhang, Y. Wang, Y. Tan, K. Xu and P. Wang, Starch-based nanospheres modified filter paper for o/w emulsions separation and contaminants removal, *Int. J. Biol. Macromol.*, 2020, **162**, 1118–1126, DOI: 10.1016/j.ijbiomac.2020.06.233.

26 A. El Manouni, F. J. Manjón, M. Mollar, B. Marí, R. Gómez, M. C. López and J. R. Ramos-Barrado, Effect of aluminium doping on zinc oxide thin films grown by spray pyrolysis, *Superlattices Microstruct.*, 2006, **39**, 185–192, DOI: 10.1016/j.spmi.2005.08.041.

27 A. R. Butt, I. A. Butt, A. Nazir, M. Ikram, S. Sadiq, K. Rashid, T. Shujah and S. Ali, Molecular imaging of CaO nanowhiskers in living organs, *Nuclear*, 2015, **52**, 159–164. https://thenucleuspak.org.pk/index.php/Nucleus/article/view/633.

28 R. Sengodan, R. Ranjithkumar, K. Selvam and B. Chandarshekar, Antibacterial activity of silver nanoparticles coated intravascular catheters (AgNPs-IVC) against biofilm producing pathogens, *Rasayan J. Chem.*, 2018, **11**, 63–68, DOI: 10.7324/RJC.2018.1111934.

29 P. M. Gonçalves, C. P. Z. Noreña, N. P. da Silveira and A. Brandelli, Characterization of starch nanoparticles obtained from Araucaria angustifolia seeds by acid hydrolysis and ultrasound, *LWT–Food Sci. Technol.*, 2014, **58**, 21–27, DOI: 10.1016/j.lwt.2014.03.015.

30 A. H. Shaffie and A. S. A. Khiar, Characterization of chitosan-starch blend based biopolymer electrolyte doped with ammonium nitrate, *AIP Conf. Proc.*, 2018, 30011, DOI: 10.1063/1.5041232.

31 I. Gul, S. M. Khan, T. Mehmood, Z. Ahmad, H. Badshah and H. Shah, Characterization of Cobalt Oxide and Calcium-Aluminum Oxide nano-catalyst through Scanning Electron Microscopy, X-ray diffraction, and Energy Dispersive X-ray Spectroscopy, *Microsc. Res. Tech.*, 2020, **83**, 1124–1131, DOI: 10.1002/jemt.23504.

32 A. Imtiaz, M. A. Farrukh, M. Khaleeq-Ur-Rahman and R. Adnan, Micelle-assisted synthesis of Almiddot;CaO nanocatalyst: Optical properties and their applications in photodegradation of 2,4,6-trinitrophenol, *Sci. World J.*, 2013, **2013**, 641420, DOI: 10.1155/2013/641420.

33 M. Mahinroosta and A. Allahverdi, Production of nanostructured γ-alumina from aluminum foundry tailing

for catalytic applications, *Int. Nano Lett.*, 2018, **8**, 255–261, DOI: 10.1007/s40089-018-0247-1.

34 Y. Y. Margaretha, H. S. Prastyo, A. Ayucitra and S. Ismadji, Calcium oxide from pomacea sp. shell as a catalyst for biodiesel production, *Int. J. Energy Environ. Eng.*, 2012, **3**, 1–9, DOI: 10.1186/2251-6832-3-33.

35 V. Sumathi, Optical Characterization of Calcium Oxide Nanoparticles, *Int. J. Adv. Technol. Eng. Sci.*, 2017, **5**, 63–67.

36 M. G. Lomelí-Ramírez, A. J. Barrios-Guzmán, S. García-Enriquez, J. de Jesús Rivera-Prado and R. Manríquez-González, Chemical and Mechanical Evaluation of Bio-composites Based on Thermoplastic Starch and Wood Particles Prepared by Thermal Compression, *BioResources*, 2014, **9**, 2960–2974, DOI: 10.15376/biores.9.2.2960-2974.

37 H. Rostami Monjezi, Z. Zarnegar and J. Safari, Starch nanoparticles as a bio-nanocatalyst in synthesis of diheteroaryl thioethers, *J. Saudi Chem. Soc.*, 2019, **23**, 973–979, DOI: 10.1016/j.jscs.2019.05.003.

38 J. Y. Xin, Y. Wang, T. Liu, K. Lin, L. Chang and C. G. Xia, Biosysthesis of corn starch palmitate by lipase novozym 435, *Int. J. Mol. Sci.*, 2012, **13**, 7226–7236, DOI: 10.3390/ijms13067226.

39 C. Kürkçü, Z. Merdan and Ç. Yamçiçier, Structural phase transition and electronic properties of CaO under high pressure, *Mater. Res. Express.*, 2018, **5**, 125903, DOI: 10.1088/2053-1591/aae012.

40 H. Gopalappa, K. Yogendra, K. M. Mahadevan and N. Madhusudhana, A comparative study on the solar photocatalytic degradation of Brilliant Red azo dye by CaO and CaMgO2 nanoparticles, *Int. J. Sci. Res.*, 2012, **1**, 91–95.

41 U. Coleto, R. A. C. Amoresi, C. A. M. Pereira, B. W. Schmidt, I. M. Iani, A. Z. Simões, E. S. Monteiro, E. Longo, M. A. Zaghete and L. A. Perazolli, Correlation of photocatalytic activity and defects generated in Ca^{2+}-based heterojunctions, *SN Appl. Sci.*, 2020, **2**, 1849, DOI: 10.1007/s42452-020-03662-6.

42 M. Serhan, M. Sprowls, D. Jackemeyer, M. Long, I. D. Perez, W. Maret, N. Tao and E. Forzani, Total iron measurement in human serum with a smartphone, in *AIChE Annu. Meet. Conf. Proc.*, 2019, pp. 1–3.

43 M. Sökmen, S. Y. Alomar, C. Albay and G. Serdar, Microwave assisted production of silver nanoparticles using green tea extracts, *J. Alloys Compd.*, 2017, **725**, 190–198, DOI: 10.1016/j.jallcom.2017.07.094.

44 J. Liqiang, Q. Yichun, W. Baiqi, L. Shudan, J. Baojiang, Y. Libin, F. Wei, F. Honggang and S. Jiazhong, Review of photoluminescence performance of nano-sized semiconductor materials and its relationships with photocatalytic activity, *Sol. Energy Mater. Sol. Cells*, 2006, **90**, 1773–1787, DOI: 10.1016/j.solmat.2005.11.007.

45 P. Martins, S. Kappert, H. N. Le, V. Sebastian, K. Kühn, M. Alves, L. Pereira, G. Cuniberti, M. Melle-Franco and S. Lanceros-Méndez, Enhanced photocatalytic activity of au/TiO2 nanoparticles against ciprofloxacin, *Catalysts*, 2020, **10**, 234, DOI: 10.3390/catal10020234.

46 Q. Zhang, W. Wang, H. Shen, H. Tao, Y. Wu, L. Ma, G. Yang, R. Chang, J. Wang, H. Zhang, C. Wang, F. Zhang, J. Qi and C. Mi, Low-Intensity Focused Ultrasound-Augmented Multifunctional Nanoparticles for Integrating Ultrasound Imaging and Synergistic Therapy of Metastatic Breast Cancer, *Nanoscale Res. Lett.*, 2021, **16**, 73, DOI: 10.1186/s11671-021-03532-z.

47 M. Ikram, T. Inayat, A. Haider, A. Ul-Hamid, J. Haider, W. Nabgan, A. Saeed, A. Shahbaz, S. Hayat, K. Ul-Ain and A. R. Butt, Graphene Oxide-Doped MgO Nanostructures for Highly Efficient Dye Degradation and Bactericidal Action, *Nanoscale Res. Lett.*, 2021, **16**(56), DOI: 10.1186/s11671-021-03516-z.

48 A. A. Fairuzi, N. N. Bonnia, R. M. Akhir, M. A. Abrani and H. M. Akil, Degradation of methylene blue using silver nanoparticles synthesized from imperata cylindrica aqueous extract, *IOP Conf. Ser. Earth Environ. Sci.*, 2018, 12018, DOI: 10.1088/1755-1315/105/1/012018.

49 A. Shahpal, M. Aziz Choudhary and Z. Ahmad, An investigation on the synthesis and catalytic activities of pure and Cu-doped zinc oxide nanoparticles, *Cogent Chem.*, 2017, **3**, 1301241, DOI: 10.1080/23312009.2017.1301241.

50 M. Aqeel, M. Rashid, M. Ikram, A. Haider, S. Naz, J. Haider, A. Ul-Hamid and A. Shahzadi, Photocatalytic, dye degradation, and bactericidal behavior of Cu-doped ZnO nanorods and their molecular docking analysis, *Dalt. Trans.*, 2020, **49**, 8314–8330, DOI: 10.1039/d0dt01397h.

51 A. Raza, M. Ikram, M. Aqeel, M. Imran, A. Ul-Hamid, K. N. Riaz and S. Ali, Enhanced industrial dye degradation using Co doped in chemically exfoliated MoS2 nanosheets, *Appl. Nanosci.*, 2020, **10**, 1535–1544, DOI: 10.1007/s13204-019-01239-3.

52 M. Ikram, M. Saeed, J. Haider, A. Haider, A. Ul-Hamid, A. Shahzadi, W. Nabgan, A. Rafique, S. Dilpazir and S. Ali, Facile synthesis of chitosan-grafted polyacrylic acid-doped CaO nanoparticle for catalytic and antimicrobial potential, *Appl. Nanosci.*, 2022, **12**, 2657–2670, DOI: 10.1007/s13204-022-02576-6.

53 Z. Mehmood, M. Ikram, M. Imran, A. Shahzadi, A. Haider, A. Ul-Hamid, W. Nabgan, J. Haider and S. Hayat, Z. officinale-doped silver/calcium oxide nanocomposites: Catalytic activity and antimicrobial potential with molecular docking analysis, *Process Biochem.*, 2022, **121**, 635–646, DOI: 10.1016/j.procbio.2022.07.035.

54 U. Ijaz, I. A. Bhatti, S. Mirza and A. Ashar, Characterization and evaluation of antibacterial activity of plant mediated calcium oxide (CaO) nanoparticles by employing Mentha pipertia extract, *Mater. Res. Express.*, 2017, **4**, 105402, DOI: 10.1088/2053-1591/aa8603.

55 S. Thakur, S. Singh and B. Pal, Time-dependent growth of CaO nano flowers from egg shells exhibit improved adsorption and catalytic activity, *Adv. Powder Technol.*, 2021, **32**, 3288–3296, DOI: 10.1016/j.apt.2021.07.015.

56 M. Ikram, A. Muhammad Khan, A. Haider, J. Haider, S. Naz, A. Ul-Hamid, A. Shahzadi, W. Nabgan, T. Shujah, I. Shahzadi and S. Ali, Facile Synthesis of La- and Chitosan-Doped CaO Nanoparticles and Their Evaluation for Catalytic and Antimicrobial Potential with Molecular Docking Studies,

ACS Omega, 2022, **7**, 28459–28470, DOI: **10.1021/acsomega.2c02790**.

57 S. Smidstrup, T. Markussen, P. Vancraeyveld, J. Wellendorff, J. Schneider, T. Gunst, B. Verstichel, D. Stradi, P. A. Khomyakov, U. G. Vej-Hansen, M. E. Lee, S. T. Chill, F. Rasmussen, G. Penazzi, F. Corsetti, A. Ojanperä, K. Jensen, M. L. N. Palsgaard, U. Martinez, A. Blom, M. Brandbyge and K. Stokbro, QuantumATK: An integrated platform of electronic and atomic-scale modelling tools, *J. Phys. Condens. Matter.*, 2020, **32**, 015901, DOI: **10.1088/1361-648X/ab4007**.

58 J. P. Perdew, K. Burke and M. Ernzerhof, Generalized gradient approximation made simple, *Phys. Rev. Lett.*, 1996, **77**, 3865–3868, DOI: **10.1103/PhysRevLett.77.3865**.

59 A. Depeursinge, D. Racoceanu, J. Iavindrasana, G. Cohen, A. Platon, P.-A. Poletti and H. Muller, Fusing Visual and Clinical Information for Lung Tissue Classification in HRCT Data, *Artif. Intell. Med.*, 2010, **50**(1), 13–21, DOI: **10.1016/j.artmed.2010.04.006**.

60 J. Heyd, G. E. Scuseria and M. Ernzerhof, Hybrid functionals based on a screened Coulomb potential, *J. Chem. Phys.*, 2003, **118**, 8207–8215, DOI: **10.1063/1.1564060**.

61 M. B. Kanoun, S. Goumri-Said, U. Schwingenschlögl and A. Manchon, Magnetism in Sc-doped ZnO with zinc vacancies: A hybrid density functional and GGA + U approaches, *Chem. Phys. Lett.*, 2012, **532**, 96–99, DOI: **10.1016/j.cplett.2012.02.055**.

62 J. F. Mammone, H. K. Mao and P. M. Bell, Equations of state of CaO under static pressure conditions, *Geophys. Res. Lett.*, 1981, **8**, 140–142, DOI: **10.1029/GL008i002p00140**.

63 V. Orazi, A. Juan, E. A. González, J. M. Marchetti and P. V Jasen, DFT study of ethanol adsorption on CaO(0 0 1) surface, *Appl. Surf. Sci.*, 2020, **500**, 144254, DOI: **10.1016/j.apsusc.2019.144254**.

64 J. Hassan, S. Naz, A. Haider, A. Raza, A. Ul-Hamid, U. Qumar, J. Haider, S. Goumri-Said, M. B. Kanoun and M. Ikram, h-BN nanosheets doped with transition metals for environmental remediation; a DFT approach and molecular docking analysis, *Mater. Sci. Eng. B Solid-State Mater. Adv. Technol.*, 2021, **272**, 115365, DOI: **10.1016/j.mseb.2021.115365**.

65 N. Shahzad, A. Hussain, N. Mustafa, N. Ali, M. B. Kanoun and S. Goumri-Said, First principles study of the adsorption and dissociation mechanisms of H2S on a TiO2 anatase (001) surface, *RSC Adv.*, 2016, **6**, 7941–7949, DOI: **10.1039/c5ra20875k**.